

Multi-Scale Model of the RF Diode Sputter Deposition of GMR Thin Films

S. Ghosal, R.L. Kosut, J.L. Ebert, A. Kozak, T.E. Abrahamson
SC Solutions, Santa Clara, CA 95054
E-mail ghosal@scsolutions.com

W. Zou, X.W. Zhou, J.F. Groves, Y.G. Yang, H.N.G. Wadley
University of Virginia, Charlottesville, VA 22903

D. Brownell, D. Wang
Nonvolatile Electronics, Inc., Eden Prairie, MN 55344

1. Introduction

Radio frequency (RF) diode sputtering deposition is a widely used process for depositing thin films and multilayers [1-3]. The development, computational implementation, and integration of the appropriate physical models for RF diode sputtering, calibrated and refined using appropriate experimental results are believed to promise a reduction of the time consuming and costly trial-and-error approach used to design, operate, and control deposition systems used for the reliable fabrication of high-quality thin metal films. To meet these objectives, a multiscale model based on the primary physical phenomena - gas flow, plasma discharge, sputtering and atom transport has been assembled to explore the RF diode deposition of thin metal films. The resulting multiscale input-output model is capable of predicting the thin-film deposition rate, the sputtered metal atoms' energy and angular distribution, both upon emission at the target and just prior to deposition at the substrate, and their sensitivity to deposition conditions such as power, working gas type, pressure, gas temperature, and electrode spacing. The metal atom flux incident upon the substrate is then used as an input to atom assembly models to deduce surface morphology and film structure. The deduced performance measures of the RF diode deposition process, such as wafer-scale uniformity of the film thickness and surface roughness of the film, in turn, influence device characteristics that utilize these films, e.g. the saturation magnetic field, and magnetoresistance of giant magnetoresistive multilayer [1].

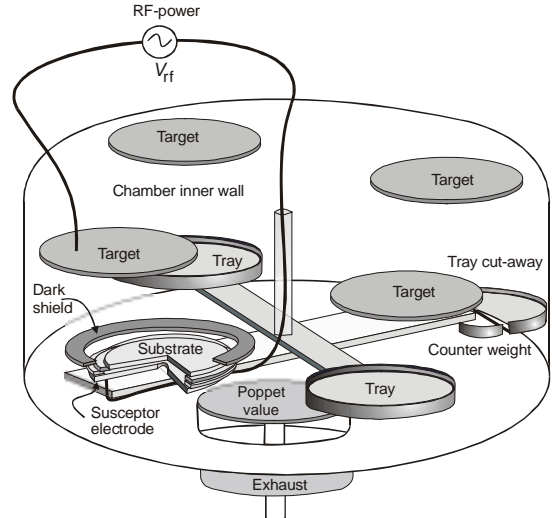


Figure 1. Schematic of the RF diode sputter chamber.

The modeling approach uses: (1) a computational fluid dynamic (CFD) finite element model to compute the velocity and pressure distribution of the working gas (argon) within a deposition chamber, (2) a one-dimensional steady-state plasma model, to determine the flux and energy of the argon ions that strike both the target and substrate, (3) results of a molecular dynamics analysis of sputtering to deduce the energy distribution, angle distribution, and sputter yield of metal atoms from the target, and (4) a Direct Simulation Monte Carlo (DSMC) model to track the propagation (and energy loss) of metal atoms through the argon working gas from the copper target to a substrate. The outputs of this sequence of models are the incident energy and angle distributions of the metal atoms at the substrate surface as functions of the working gas pressure, temperature, and the plasma power. A two dimensional, hyperthermal kinetic Monte Carlo model is then used to relate the film surface morphology and atomic scale structure to the flux parameters and therefore the conditions of the vapor deposition process. The individual models for gas flow, plasma discharge, sputtering, metal atom transport, and kinetic Monte Carlo models developed for copper are then integrated to create a detailed, steady-state, input-output, multiscale model.

The menu is organized as follows. The RF diode sputtering process, experimental results, and the reactor scale models of interest for metal thin-film fabrication are briefly

* Acknowledgements

This work was supported by the Applied Computation and Mathematics Program at Defence Advanced Research Projects Agency (DARPA). Dr. A. Tsao was the program manager.

reviewed in Section 2. The development of model and relevant results for the fluid flow, the plasma, the sputtering, the vapor phase atom transport, and film growth are addressed in Sections 3, 4, 5, 6, and 7 respectively. A detailed integrated, steady-state, input-output model for RF diode sputtering for growing thin metal films that results from the integration of these individual models is described in Section 8. An approximate coarse grained input-output version of the detailed model provides reasonable predictions of process performance several orders-of-magnitude faster than the detailed model, and is described in this section. The coarse grained model, when refined and validated with experimental data, is shown to be useful for performance sensitivity analysis of deposition rate and uniformity with respect to input power, pressure, temperature, and electrode spacing. Sensitivity results are given in Section 8. Dependence of measured surface morphology on plasma power and background pressure was correctly predicted by the models. In Section 9, we show how these sensitivity results can be used to derive set-point control tolerances for the critical thin-film layer in an actual diode-sputtering process. Finally, Section 10 describes how deposition uniformity was substantially improved by target shaping, a process modification resulting directly from the simulation studies that successfully passed all the qualification tests needed to incorporate a modification into NVE's regular manufacturing process.

2. The RF Diode Deposition Process

A schematic diagram of an RF diode sputter chamber is shown in Figure 1. The chamber depicted in this figure represents the essential elements of a Perkins Elmer 2400 sputtering system at Nonvolatile Electronics (NVE) where all the experiments were performed. Copper was chosen for this study because it is commonly used as the conducting layer in several giant magnetoresistive applications [1-3]. The copper target for sputtering was mounted at the top of the chamber while the wafer on which the thin film is deposited is mounted at the bottom. Although four targets are present in the chamber during multilayer processing, only the target directly above the substrate is active during the deposition of a layer. Argon gas at low pressure (20-50 mTorr) flows continuously through the chamber. An RF plasma discharge is generated and maintained between the target electrode and the wafer (substrate) electrode by means of a power supply and RF matching network. Argon ions formed in the plasma bombard the copper target and result in copper atom ejection, which propagate through the argon and are deposited on the wafer substrate.

A systematic series of experiments was conducted to explore the effect of pressure and power on the surface topography. The (background) working gas in the RF diode sputtering chamber was argon at a temperature of 300 K. The spacing between the sputter target and deposition substrate was 3.81 cm. The substrate consisted of a 2000 Å amorphous silicon nitride film grown on a silicon wafer by chemical vapor deposition. The RMS roughness of the silicon nitride film was approximately 1.5 Å. A copper film of 2000 Å was then

deposited over the silicon nitride film. The background pressure and input power were independently varied keeping the film thickness constant. The resulting surface images and RMS roughness, for a scanned area of 2 μm by 2 μm, were experimentally obtained using an Atomic Force Microscope (AFM), as shown in Figure 2.

To study the effect of pressure on surface morphology, the input power was held constant at 175 W and the background pressure was varied from 10 mTorr (1.33 Pa) to 50 mTorr (6.65 Pa). AFM images of the copper surface corresponding to pressures of 10 and 50 mTorr are shown in Figures 2 (a), and (b), respectively. They show that an increase in the background pressure causes an increase in surface roughness. The trend is more clearly shown in Figure 2 (e). To study the effect of input power on surface morphology, the background pressure was held constant at 20 mTorr and the input power was varied from 50 to 350 W. AFM images corresponding to input powers of 50 W and 350 W are shown in Figures 2 (c) and (d), respectively. These surface images show that an increase in input power causes a decrease in surface roughness, a trend clearly seen in Figure 2 (f).

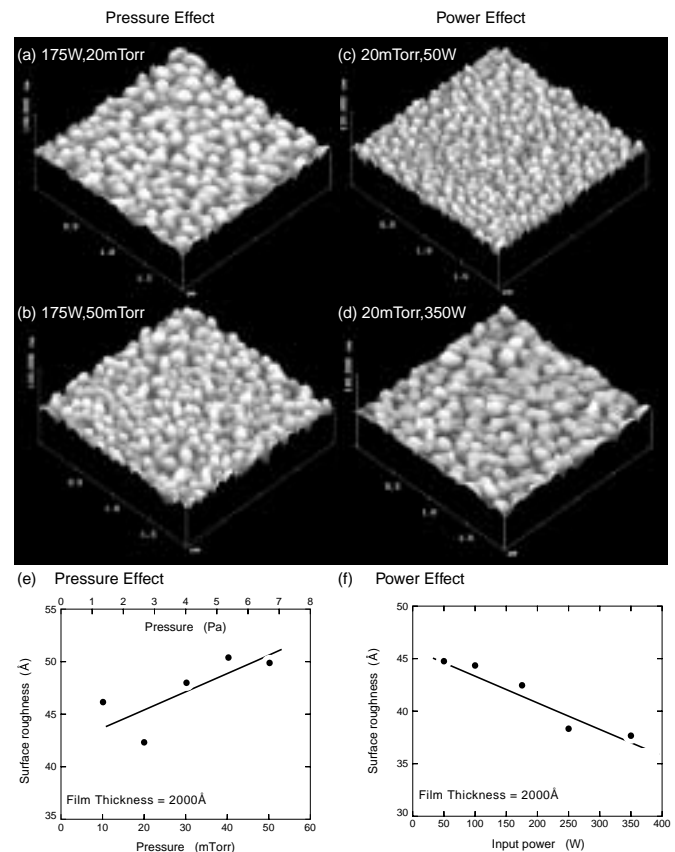


Figure 2. Atomic force micrographs of 2000Å thick copper films grown at various pressures and input powers showing the dependence of surface roughness upon pressure and power.

The following physical models were developed and integrated in order to link the process conditions to the properties of the resulting copper thin film (see Figure 3 (a)):

- (1) A computational fluid dynamic (CFD) finite element model was used to deduce the velocity and pressure distribution of the argon gas flow in the chamber.

- (2) A 1D steady-state plasma model was used for the Ar ion flux and energy striking the target and the substrate,
- (3) A molecular dynamics (MD) sputtering model was used to determine the energy distribution, angle distribution, and yield of the copper atoms sputtered from the target by the Ar ions.
- (4) A Direct Simulation Monte Carlo (DSMC) model using binary collision theory (BCT) was used for the transport of copper atoms through the low-pressure argon gas to the deposition substrate.
- (5) The outputs of the DSMC transport model were used as inputs in a 2-D kinetic Monte Carlo (KMC) model to simulate film morphology under various deposition condition.

The input variables for the models are the applied power, P (W), gas pressure, p (mTorr), gas temperature, T (K), and the electrode spacing, l (cm). The output variables are deposition rate, d ($\text{\AA}/\text{min}$), thickness uniformity, σ , radial distribution of the deposited copper atoms on the substrate, $\phi(r)$, and the copper flux, Γ (atom/sec) on the substrate. Figure 3(a) depicts the inputs and outputs of each of the individual models. These component models can be chained to create a multiscale, integrated model as shown in the flow chart of Figure 3 (b), and from a higher level view in Figure 3(c).

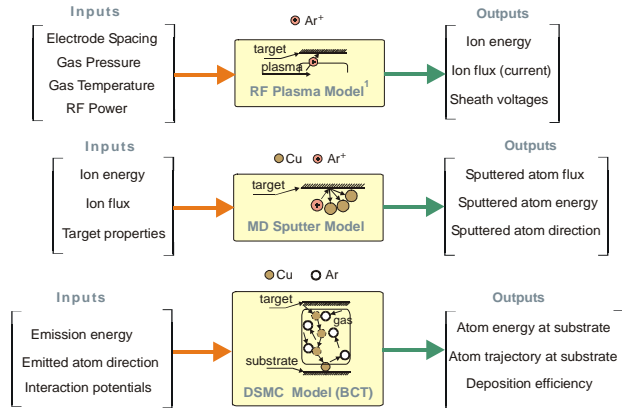


Figure 3 (a). Inputs and outputs corresponding to the various physical models.

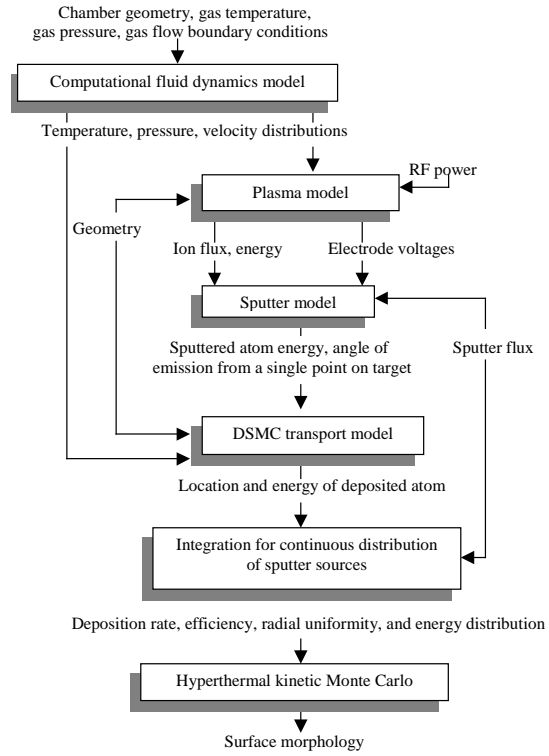


Figure 3(b). Flow chart showing the inter-relationships between the physical models.

3. Fluid Flow Model

A computational fluid dynamic (CFD) model was constructed to simulate the argon flow in the chamber and yielded the resulting convective gas velocity and pressure distributions. The principal physical equations governing the flow of a viscous compressible gas flow are the continuity, momentum, and state equations. The finite element method was used to solve these equations. as given in [4].

The vector continuity equation for compressible gas flow is

$$\nabla \cdot (\rho \mathbf{V}) + \frac{\partial \rho}{\partial t} = 0 \quad (3.1)$$

where ρ is the density of the fluid, and \mathbf{V} the velocity vector at a generic point (x, y, z) in the fluid.

The vector Navier-Stokes momentum equation for the compressible gas flow is

$$\frac{D(\rho \mathbf{V})}{Dt} + \nabla p = \nabla^2 (\mu \mathbf{V}) + \mathbf{F} \quad (3.2)$$

where D/Dt represents the substantial derivative with respect to time t ; \mathbf{V} , p , and \mathbf{F} are, respectively, the velocity vector, pressure, and the resultant external force vector at a generic point (x, y, z) in the fluid.

The equation of state for the compressible flow based on the assumption of a perfect gas is

$$\rho = p / (RT) = p / [(C_p - C_v) T] \quad (3.3)$$

where T is the temperature of the gas, R is the universal gas constant, and C_p , C_v are, respectively, the specific heats of the gas at constant pressure and constant volume.

Both incompressible and compressible viscous fluid flow models were developed using ADINA-F, a commercial finite-element software package, and then used to simulate the gas flow inside the chamber. The 3-D finite-element mesh for one-half of the chamber is shown in Figure 4. Figure 5 shows the vertical profiles of argon speed between the target and the substrate at the three centerline locations marked in top (cross-sectional) view shown in the lower part of the same figure.

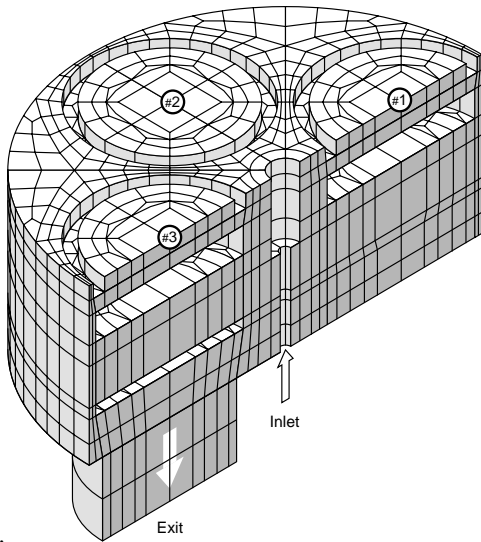


Figure 4. Three dimensional finite element mesh of half of the sputter chamber.

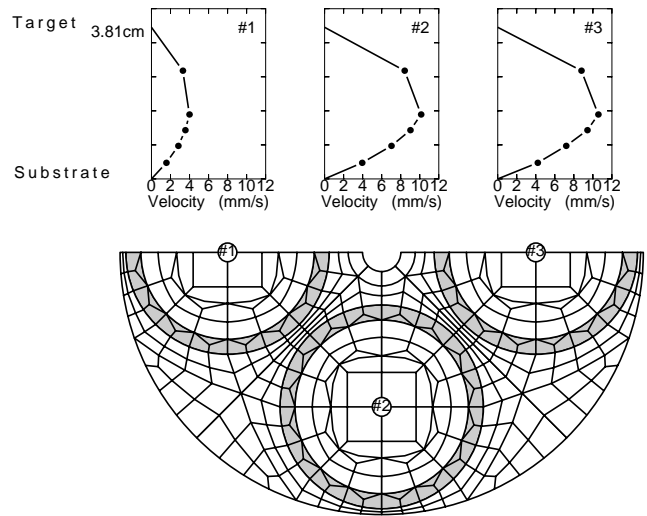
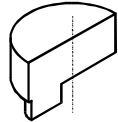
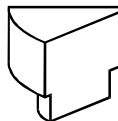


Figure 5. Working gas velocities across the centerline between target and substrate.

It is noted that because of symmetry in the chamber geometry and the boundary conditions, it is sufficient to work with one-half and one-eighth of the actual chamber for the mesh refinement analyses shown in Table 1. Extensive mesh refinement studies for tetrahedral and hexahedral finite elements as well as for incompressible and compressible flow were performed to establish the convergence of the finite element solutions and therefore the fidelity of the simulations. The different cases that were considered for mesh refinement studies are summarized in Table 1. Based on numerical simulation results such as those shown in Figure 5, the maximum magnitude of the bulk (convective) gas velocity in the region of interest between the electrodes is approximately 0.01 m/sec, and the pressure inside the chamber is approximately constant, with variations of less than 0.01% of the mean pressure.

Table 1. Comparison of various models and finite element schemes for fluid flow analysis.

##	scheme of region under analysis	fluid flow model	type of finite elements (amount of unknowns)	comments
1	 1/2 model	viscous incompressible fluid	hexahedral 27 node 3D elements (65,971)	main model
2	 1/8 model	viscous incompressible fluid	hexahedral 27 node 3D elements (17,210)	“coarse” model for mesh refinement study
3		viscous incompressible fluid	hexahedral 27 node 3D elements (134,606)	“refined” model for mesh refinement study
4		viscous compressible fluid	tetrahedral 4 node 3D elements (21,215)	model for study of influence of fluid compressibility
5		viscous compressible fluid	tetrahedral 4 node 3D elements (149,300)	“refined” model for mesh refinement study of compressible flow

4. Plasma Model

The primary function of the steady-state plasma model is to predict the flux and energy of argon ions striking the target and the substrate for specified values and ranges of input variables such as applied power and gas pressure.

A schematic diagram of the chamber used for the purpose of plasma modeling is shown in Figure 6. The input RF power, P_{abs} , applied to the target electrode, a , and the substrate electrode, b , (see Figure 6), results in the formation of the bulk plasma (between the electrodes) containing an equal density, n_o , of Ar ions and electrons, with thin “electron-free” regions called sheaths near each electrode. For the range of pressures of interest, 20-50 mTorr, the mean free path of the Ar ions is less than the sheath thickness implying that the ions are subject to one or more collisions as they traverse the sheath. For this reason, the sheath is said to be “collisional”. Two important sets of variables characterizing the plasma are the sheath thicknesses, s_{ma} , and s_{mb} , and the voltages, V_a and V_b , of sheath a and sheath b , respectively.

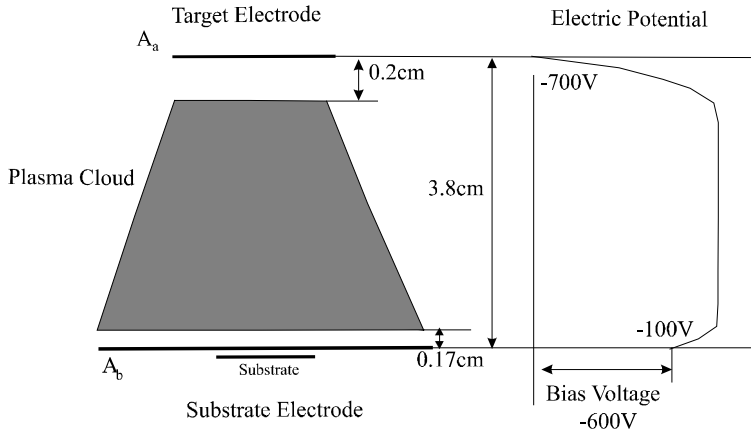


Figure 6. Computed electric potential between the target and substrate as calculated from the one-dimensional plasma model. The argon gas temperature, electrode spacing and input RF power were 300 K, 3.81 cm, and 175 W, respectively.

The inputs to the plasma model are p , the argon gas pressure (Torr); P_{abs} , the input power (W); l , the distance between electrodes (m); A_a , the target electrode area (m²); A_b , the substrate electrode area (m²); T , the gas temperature (K); ω , the rf current frequency (rad/sec); A_s , the area of the substrate (m²) on which the film grows. The nominal values of the inputs to the plasma model were: $p = 20$ mTorr, $P_{abs} = 175$ W, $l = 1.5$ in = 0.038 m, $A_a = 324$ cm², $A_b/A_a = 1.5$, $T = 400$ K, $\omega = 13.86$ MHz, $A_s = 81$ cm².

Expressions for physical variables of interest in plasma discharge analysis such as the mean free path, λ_r , of the Ar ions, the electron-neutral Ar collision frequency ν_m , the sheath size, and the ratio (n_s/n_o) of Ar ions at the sheath edge to the Ar ions in the bulk plasma are given in [5]. A “self-consistent” uniform symmetric model for a capacitive parallel-plate RF plasma discharge given in [5] has been extended here to the asymmetric case of unequal target and substrate area as

described below. The simplifying assumptions made in the formulation of the self-consistent model are given in [5]. The average sheath voltages, \bar{V}_a and \bar{V}_b , are related to the areas of the sheath:

$$\bar{V}_a / \bar{V}_b = (A_b / A_a)^q \quad (4.1)$$

Here the exponent q can typically take values between 1.5 and 4 depending on operating conditions [2, 4], and was used to calibrate the model. A value of 2.5 was found to provide good correlation with experiments for the range of pressure, power, and temperature discussed.

The outputs of interest, the Ar ion flux and the Ar ion energy, are computed from a nonlinear algebraic model based on three energy balances. The first energy balance accounts for the fact that the RF power, P_{abs} , supplied to the plasma result in plasma heating. As a result,

$$P_{abs} = S_{abs,a} A_a + S_{abs,b} A_b \quad (4.2)$$

where $S_{abs,a}$ and $S_{abs,b}$ are the power loss per unit area corresponding to sheath a and sheath b , respectively, and A_b and A_a are the areas of sheath a and b , respectively. Other energy balance equations were considered, which more closely matched the equations from [5] for the symmetric electrode system (average power dissipation over the system instead of separate dissipation at each sheath), but the separate system of Equation 4.2 was found to provide better correlation with experiments. The second energy balance relates to the power loss per unit area at each sheath, $S_{abs,a}$ and $S_{abs,b}$. (For simplicity, the subscripts a and b are omitted below.) For each sheath, E_t , the total energy lost per ion lost from the system, is given by:

$$E_t = E_c + 2T_e + E_i \quad (4.3)$$

Here, E_c is the collisional energy lost per creation of an electron-ion pair, $2T_e$ is mean kinetic energy lost per electron striking the electrode (based on a Maxwellian distribution), and E_i is the mean kinetic energy per ion striking the electrode. The ion current density J at each sheath is given by:

$$J = e n_s u_s \quad (4.4)$$

where e is the charge on an electron, n_s the density of Ar ions at the sheath edge, and u_s the velocity of the ions at the sheath edge. The power loss per unit area, S_{abs} , corresponding to each sheath is

$$S_{abs} = J E_t = e n_s u_s (E_c + 2T_e + E_i) \quad (4.5)$$

For a collisional sheath,

$$E_i = \bar{V} = 0.78 V_1 \quad (4.6)$$

Here \bar{V} is the average sheath voltage, and V_1 is the peak sheath voltage.

The third energy balance for electron power loss S_e is that part of the total power-loss S_{abs} associated with all collisions involving electrons, and is given by

$$S_e = e n_s u_s (E_c + 2T_e). \quad (4.7)$$

S_e is attributable to ohmic heating in the bulk plasma $S_{ohm,p}$, ohmic heating in the sheath $S_{ohm,s}$ and stochastic heating in the sheath $S_{stoc,s}$. In terms of these quantities S_e can be expressed as follows [5]:

$$S_e = S_{ohm,p}/2 + S_{ohm,s} + S_{stoc,s} \quad (4.8)$$

Combining equations (4.5) - (4.8), we obtain for each sheath

$$S_{abs} = (S_{ohm,p}/2 + S_{ohm,s} + S_{stoc,s}) \left[1 + \frac{\bar{V}}{E_c + 2T_e} \right] \quad (4.9)$$

Equation (4.9) can then be used in equation (4.2), once for each sheath. The basic parameters and variables for the plasma discharge enter equation (4.2) through the following nonlinear equations for $S_{ohm,p}$, $S_{ohm,s}$, and $S_{stoc,s}$.

The ohmic heating $\bar{S}_{ohm,p}$ in the bulk plasma is given by

$$\bar{S}_{ohm,p} = \alpha \tilde{V} d, \quad (4.10)$$

where

$$\alpha = 1.73(m/2e)(n_s/n_0)\epsilon_0\omega^2\nu_m T_e^{0.5} \quad (4.11)$$

$$\tilde{V} = V_{a1}^{0.5} + V_{b1}^{0.5} - (V_{a1}V_{b1})^{0.25} \quad (4.12)$$

Here, m = mass of the electron, e = charge on the electron, ϵ_0 = permittivity of vacuum, n_s = ion density at the sheath edge, n_0 = ion density in the bulk plasma, ω = RF frequency, ν_m = frequency of collisions between electrons and neutral Ar atoms, T_e = electron temperature (volts), and d = thickness of the plasma. The ohmic heating in the sheath is given by

$$\bar{S}_{ohm,s} = \alpha V_1^{0.5} s_m \left[0.235 (V_1/T_e)^{0.5} + 1.16 + 4.39 (T_e/V_1)^{0.5} \right] \quad (4.13)$$

Here α is given by (4.11).

The stochastic heating in the sheath, $\tilde{S}_{stoc,s}$ is given by

$$\tilde{S}_{stoc,p} = 0.61 (m/e)^{0.5} \epsilon_0 \omega^2 T_e^{0.5} V_1 \quad (4.14)$$

Here V_1 is the peak voltage across the sheath. The iterative process used to solve for the sheath thicknesses and sheath voltages, Ar ion densities, and Ar ion velocities is described in [5]. The equations for these parameters are coupled, and can not be solve in a closed form solution. These equations are nearly unchanged from those proposed in [5]. The output quantities of interest from the plasma model are J , the ion current, given by (4.4), and ϵ_{ic} , the energy of the ions when they strike the electrode, given by

$$\epsilon_{ic} = 0.62 (\lambda_i/s_m) \bar{V} \quad (4.16)$$

Here λ_i is the mean-free path of the ions. The set of non-linear equations described above constitute the steady-state plasma model. It was solved using Xmath, part of the MATRIX_xTM commercial package used for systems and controls simulation [6]. The plasma model was calibrated using experimental results on NVE's RF diode-sputtering chamber. Figure 7 shows a comparison of plasma model

predictions and experimental data for the bias voltage across the electrodes, which is the magnitude of the difference between the two sheath voltages, as a function of pressure and input RF power, after adjusting (or calibrating) the model (proper choice of the value of the exponent q in Equation 4.1, etc.).

Model simulation results shown in Figure 8 indicate that increasing the input power significantly increases the ion current density (or ion flux) and ion energy. Figure 9 shows that increasing the pressure slightly increases the ion current density (or ion flux) while significantly decreasing the ion energy. Several other useful plasma model simulation results are documented in [5].

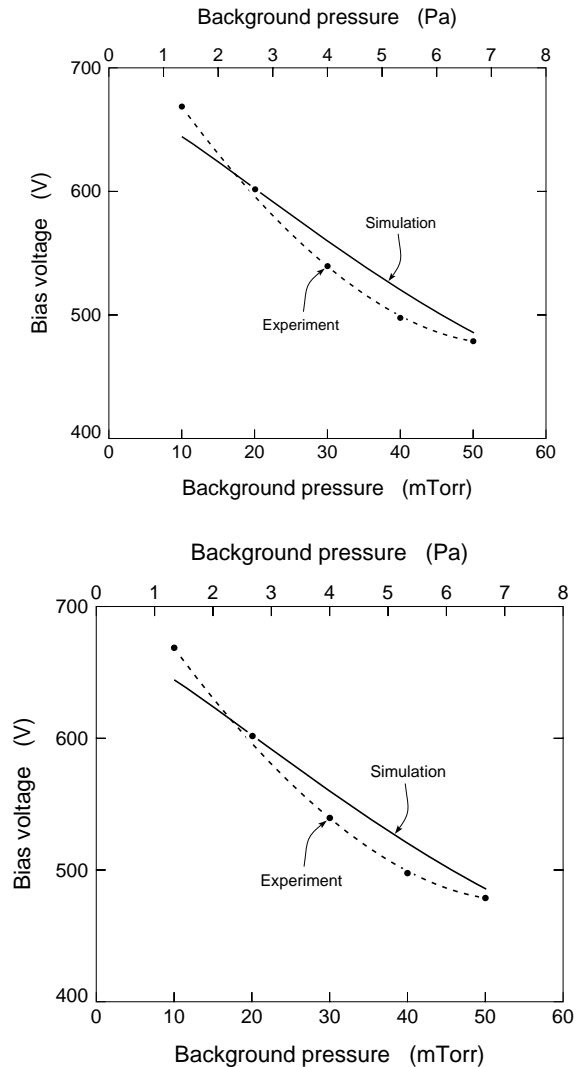


Figure 7. Experimental validation of the plasma model showing predicted and measured bias voltages at various chamber pressures and RF powers. The argon gas temperature and electrode spacing were 300 K and 3.81 cm, respectively.

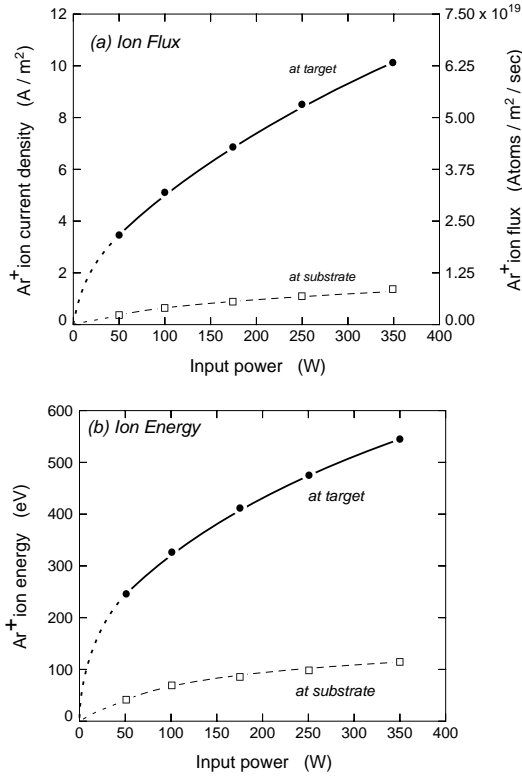


Figure 8. Plasma model results showing the effect of power on Ar⁺ ion current density and Ar⁺ ion energy at the target and the substrate.

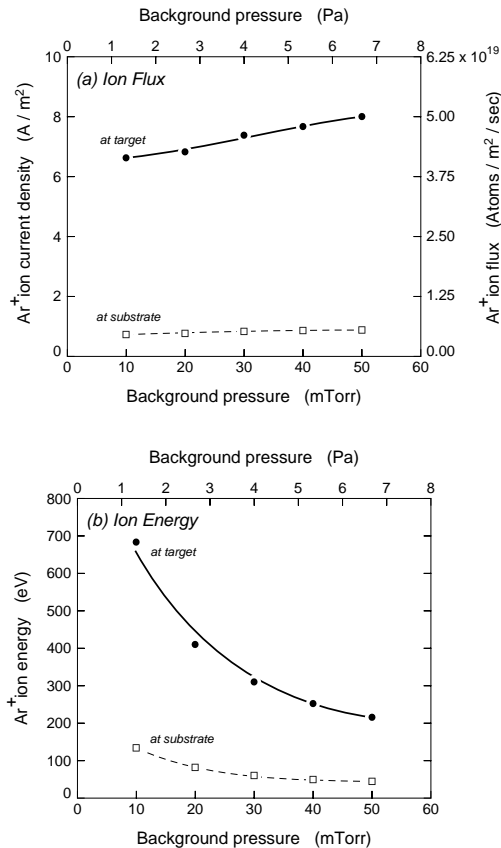


Figure 9. Plasma model results showing the effect of pressure on Ar⁺ ions current density and on energy at both the target and the substrate.

5. Sputter Model

When energetic Ar ions bombard a copper target, some of the atoms are sputtered (ejected) from the copper surface. To analyze this process, the Ar ions were modeled using a universal potential [15]. An embedded atom potential method was used to model the interaction forces between the copper atoms in a (111) flat single crystal target. The sputter yield, Y , and the distribution of the energy, ϵ_{cu} , and angle, α_{cu} , of the sputtered copper atoms as a function of the energy, ϵ_i , and incident angle, θ , of the Ar ions striking the target were computed using a molecular dynamics sputter model that simulates Ar impacts with the copper target [7]. The model also takes into account the effect of the texture of the target surface. The inputs to the sputter model are the ion current density J_i , and the mean ion impact energy ϵ_{ic} , which are the outputs of the plasma discharge model.

The ion energy, ϵ , was fitted to a Rayleigh distribution [6] with mean value, ϵ_{ic} , equal to the ion energy computed in the plasma model:

$$P(x) = xe^{-x^2/2} \quad (5.1)$$

Here, $x = \epsilon/\epsilon_{ic}$ is the ratio of the incident ion energy to the computed mean ion energy.

The sputter yield, $Y(\epsilon_i, \theta)$, i.e., the number of copper atoms sputtered by each argon ion, is given by [6],

$$Y(\epsilon_i, \theta) = \begin{cases} 0, & \theta > \theta_m \left(\frac{270 - \theta_0}{90 - \theta_0} \right)^{1/\lambda} \\ a \cdot \exp \left[- \left(\frac{\alpha}{\epsilon_i} \right)^\beta \right] \left\{ 1 + \sin \left[\theta_0 + (90 - \theta_0) \left(\frac{\theta}{\theta_m} \right)^\lambda \right] \right\}, & \theta < \theta_m \left(\frac{270 - \theta_0}{90 - \theta_0} \right)^{1/\lambda} \end{cases} \quad (5.2)$$

Here, $\theta_m = 50.0^\circ$, $\theta_0 = 19.9^\circ$, $\lambda = 3.23$, $a = 3.7$, $\alpha = 360.0$, and $\beta = 0.85$.

The break point angle for the sputter function is 74° . This equation can be conveniently separated into two parts, one depending on the ion energy, and the other depending on the incident angle. Ignoring large angles, we have:

$$Y(\epsilon_i) = a \cdot \exp \left[- \left(\frac{\alpha}{\epsilon_i} \right)^\beta \right] \quad (5.3)$$

$$Y(\theta) = 1 + \sin \left[\theta_0 + (90 - \theta_0) \left(\frac{\theta}{\theta_m} \right)^\lambda \right] \quad (5.4)$$

Figure 10 shows the sputter yield of copper as a function of the input ion energy, and the (probability) distribution of the sputtered atom energies, which is independent of ion energy and angle. Probability density functions for the angle α_{cu} of the sputtered copper atoms are given in [6].

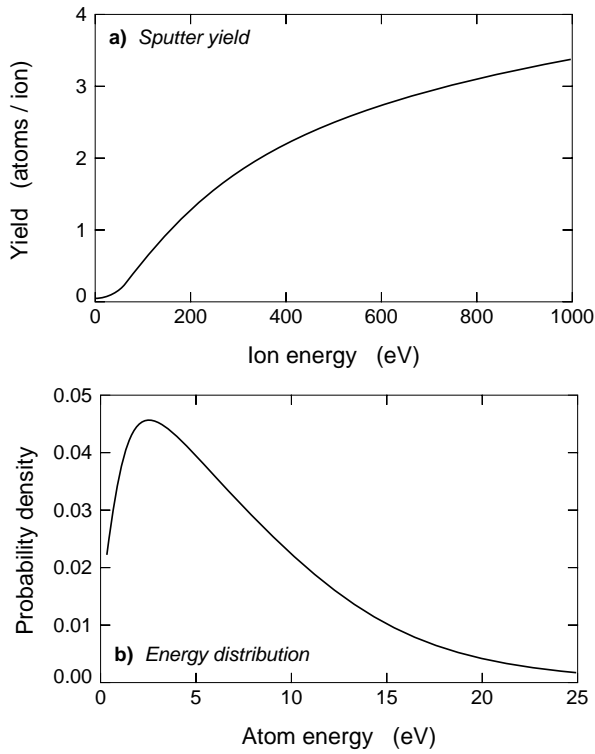


Figure 10. Results of molecular dynamics calculations for (a) sputter yield and, (b) sputter atom energy distribution.

6. DSMC/BCT Transport Model

An atomistic scale DSMC model based on three-dimensional biatomic collision theory (BCT) was developed for simulating the transport of copper atoms inside the low-pressure argon chamber [8]. The BCT code tracks individual metal atoms through the background gas from the sputtering target (source) to deposition substrate with the atom trajectories being determined by binary collisions. The code follows copper atoms one at a time from the sputtering target to the substrate or out of the modeled volume. During transport modeling, copper atom collisions with individual “background” Ar gas atoms are simulated at intervals determined from mean free path calculations, with each collision event being treated as an elastic, momentum transferring event which changes the velocity vector of the copper atom. The model simulates a neutral, monoelemental, monatomic background gas atom interacting with a neutral, monoelemental, monatomic sputtered atom. The physical and computational details of the DSMC/BCT model can be found in [8]. The key calculations of the model, shown as a flow diagram in Figure 11 and briefly described below, are (a) computation of the mean free path, and (b) calculation of the copper atom velocity vector following a collision with the background gas atom.

The assumptions associated with the DSMC/BCT model are:

- The copper - argon interactions are purely elastic.
- The directed momentum transfer cross-section employs the purely repulsive Universal Potential to describe copper - argon interaction.
- Argon energy follows Maxwell-Boltzmann distribution.

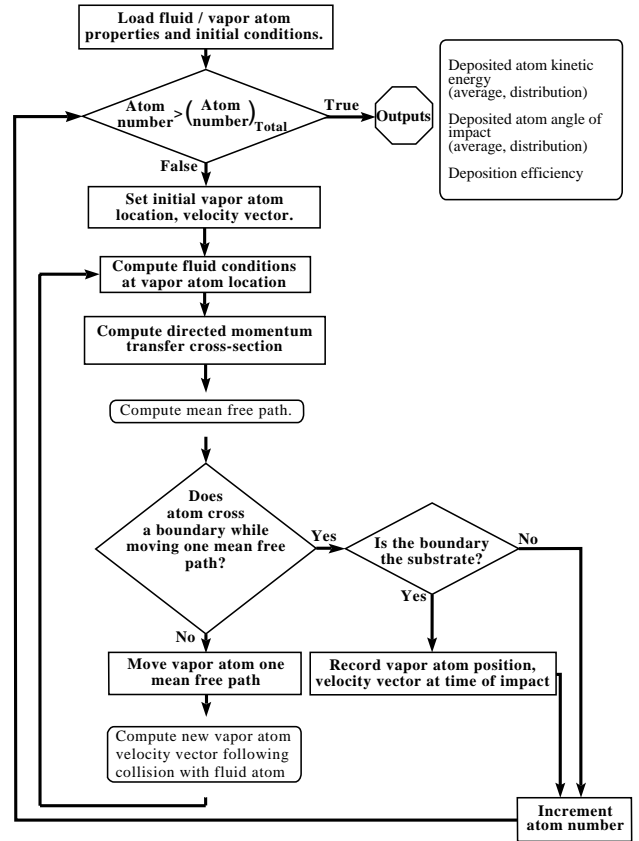


Figure 11. Flow chart for Direct Simulation Monte Carlo model for sputter atom transport.

The point at which a collision between the sputtered atom and the background gas atom occurs can be determined from a calculation of the atom’s mean free path λ , which, for an atom traveling in a gas whose velocity distribution follows a Maxwell-Boltzmann distribution, is given by [9]

$$\lambda = \frac{RT}{\sqrt{2}pN_A\sigma_d} \quad (6.1)$$

Here, R is the Universal gas constant (8.3145 J/(mol K)), T is the average carrier gas temperature along the copper atom’s path of travel (K), p is the average carrier gas pressure along the copper atom’s path of travel (Pa), N_A is Avogadro’s number (6.0221×10^{23} atoms/mol), and σ_d is the directed momentum transfer cross-section for the specific gas/sputtered atom combination. While equation (6.1) provides the *mean* free path, the actual distance between two successive collisions shows a statistical spread described using a Poisson distribution [10, 11],

$$P_{collision} = \frac{1}{\lambda} e^{-x/\lambda} dx \quad (6.2)$$

The above expression, used in the BCT model, yields the probability of a collision occurring when an atom moves from distance x to $x + dx$.

Of the variables included in equation (6.1), σ_d is the most difficult to determine. The directed momentum transfer cross-section of equation (6.1) is defined below [12-14].

$$\sigma_d = 2\pi \int_0^\pi (1 - \cos x) \sigma(x) \sin x dx \quad (6.3)$$

Here, χ is the deflection angle for either atom in the center of mass (CM) reference frame [9], and $\sigma(\chi)$ is the angular differential cross-section. Since an exact solution of equation (6.3) cannot be readily obtained, the following approximation for σ_d was used [7, 15]:

$$\sigma_d \cong \pi (b_{\max})^2 \quad (6.4)$$

Here, b_{\max} is the atomic separation at which a Cu-Ar interaction generates an angular deflection in the trajectory, χ , of 0.01 radians. Determination of b_{\max} subsequently yields σ_d and λ following a collision [8].

The second major calculation of the BCT model involves determination of the copper atom velocity vector after collision with an argon atom. The velocity vector for the copper atom after a collision is given by [16]:

$$\mathbf{U}_{va} = \frac{m_c |\mathbf{U}_r| \hat{n}_0}{m_c + m_v} + \frac{m_v \mathbf{U}_v + m_c \mathbf{U}_c}{m_c + m_v} \quad (6.5)$$

Here, the first term represents the copper atom's new CM velocity vector and the second term represents the velocity of the center of mass. The velocity vectors of the two atoms prior to the collision event (\mathbf{U}_c , \mathbf{U}_v), the relative velocity of those atoms (\mathbf{U}_r), the mass of the atoms (m_c , m_v), and the form of the interaction potential $V(r)$ represent the critical inputs to equations. The determination of the unit vector \hat{n}_0 , the direction of travel of the copper atom in the CM system after the collision, depends upon the interaction potential used. The details of the determination of \hat{n}_0 are provided in [8].

Results of sputter atom transport simulation obtained using the DSMC/BCT model are shown in Figures 12-14. In Figure 12, the deposition efficiency is defined as the fraction of total number of atoms sputtered from the target surface that actually reach the wafer surface. Figure 12 shows simulation results for different conditions of gas pressure p , gas temperature T , and electrode spacing l . It is seen that the deposition efficiencies for various operating conditions all lie on a single curve when plotted against a single parameter pl/T . This reason for this data collapse is that the deposition efficiency decreases as the number of collisions undergone by the sputter atom increases. The number of collisions is proportional to l , the electrode spacing as well as to the density of the gas, which in turn is proportional to p/T . Therefore, the number of collisions is proportional to the product of p/T and l , the abscissa of the graph shown in Figure 12, and as pl/T increases, the deposition efficiency decreases. The radial distribution of copper atoms arriving at the wafer surface is a measure of the uniformity of the thin-film deposited. The two variables that have an effect on this radial distribution are electrode spacing and pressure. Ideally, uniformity would be maximized if the atoms was

sputtered normal to the target (and wafer) surface and did not undergo any collision along its path. Figure 13(a) shows that uniformity improves with decreasing electrode spacing because the atoms undergo fewer collisions as a result of reduced path length. Figure 13(b) shows that uniformity improves slightly with increasing pressure. If one considers emission from a single point on target, the spread of the (deposited) atom flux profile, $f(r)$, on the wafer is narrower at higher pressures because of shortened mean free paths. When this narrower profile obtained from single-point emission at higher pressures is integrated over the entire target surface, the result is a more uniform deposition distribution. Complete uniformity would be reached in the limit as the width of $f(r)$ approached zero.

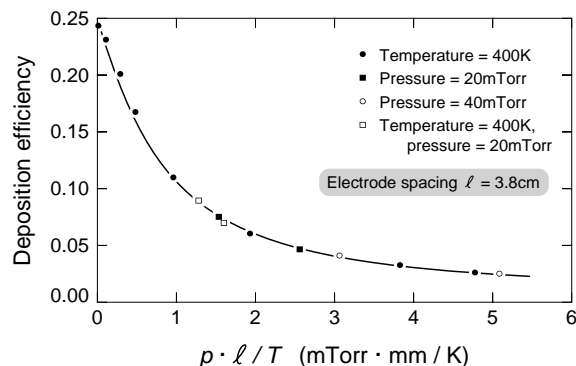


Figure 12. Deposition efficiency of sputtered copper calculated using the DSMC transport model.

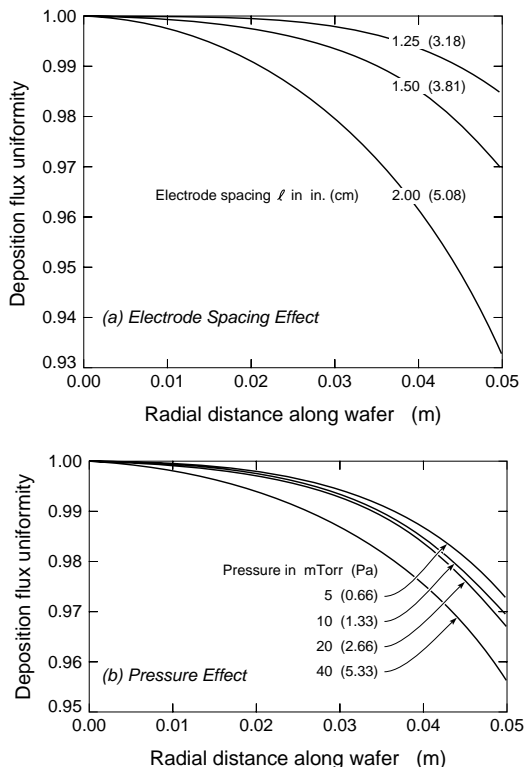


Figure 13. Sputtered atom deposition flux distribution as function of electrode spacing and chamber pressure.

Figure 14 shows the distribution of energy of the sputter atoms reaching the substrate at various pressures. The energy scale is logarithmic in order to show more clearly the bimodal nature of some of the distributions. At low pressures (below 5 mTorr), the energy distribution is distinctly bimodal. One of the modes is close to the mean emission energy of the sputter atoms (5.1 eV), while the other mode is close to the mean energy of thermalized atoms at the gas temperature of 400K (0.034 eV). Thus, it is seen that at pressures below 5 mTorr, typical of magnetron sputtering, a significant fraction of the atoms retain the relatively high sputter emission energies. However, at pressures 10 mTorr and above, typical of diode sputtering, most of the sputtered atoms reaching the wafer are thermalized.

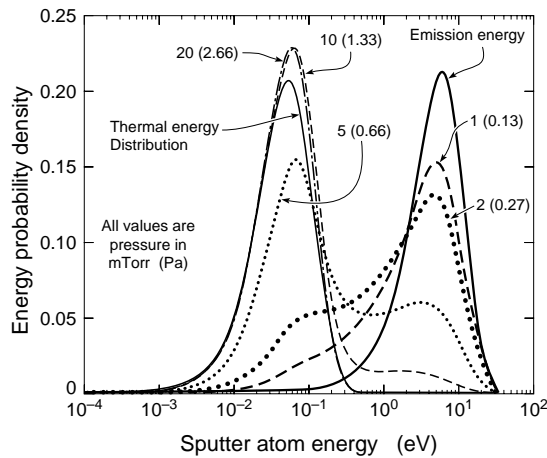


Figure 14. Energy probability density distributions for copper atoms incident upon a substrate at various pressures. The argon gas temperature, electrode spacing and input RF power were 300 K, 3.81 cm, and 175 W, respectively

Finally, Figure 15 shows the average energies and relative fluxes of Ar^+ ions and Cu atoms when a single Cu atom, re-sputtered from the substrate, reaches the target. At a sputter efficiency of three, 27,000 high-energy Ar^+ ions at 670 eV result sputter 81,000 Cu neutral atoms from the target. Of these neutrals, less than 29,000 reach the substrate with the rest returning to the target after undergoing multiple collisions. The overwhelming majority of these atoms are thermalized with a median

energy of 0.1 eV, with a small number (970) having a median energy of 3 eV. Because the substrate is at a potential lower than that of the plasma, some energetic Ar^+ ions at 60 eV hit the substrate causing re-sputtering of the copper atoms that have been deposited. Again, most of these re-sputtered atoms undergo collisions and are re-deposited on the substrate.

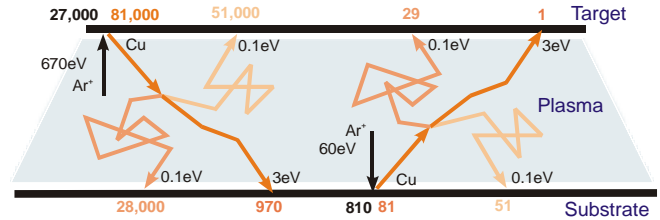


Figure 15. Energies and relative fluxes of argon ions and sputtered copper atoms for RF diode sputtering at 10 mTorr, the rest of the conditions being at nominal values. The atom trajectory following each collision is shown in a fainter shade.

7. KMC Model

The energy and incident angle distributions of the metal atom flux were used as inputs to a 2-D hyperthermal KMC model to predict surface morphology [17]. In this approach, hot atom effects are pre-computed using molecular dynamics methods [18, 19]. As an atom of defined velocity reaches the growth surface, the MD results are used to instantaneously implement hot atom effects such as reflection, re-sputtering, bias and athermal diffusion. A multipath KMC algorithm then computes atomic hopping before the next atom arrives [17]. Figure 16 (a) and (b) show the computed surface morphology when either the process power or pressure was varied. Note that these resulted in changes in both the atom energy and angular distribution and the deposition rate. This study reveals that the roughness of copper films increased as the plasma power is decreased and/or the background pressure is increased. A comparison of roughness between experiments and simulations is shown in Figure 17. The experimental data and simulation results were normalized at the first data point. It is seen that the trends are correctly predicted by the model.

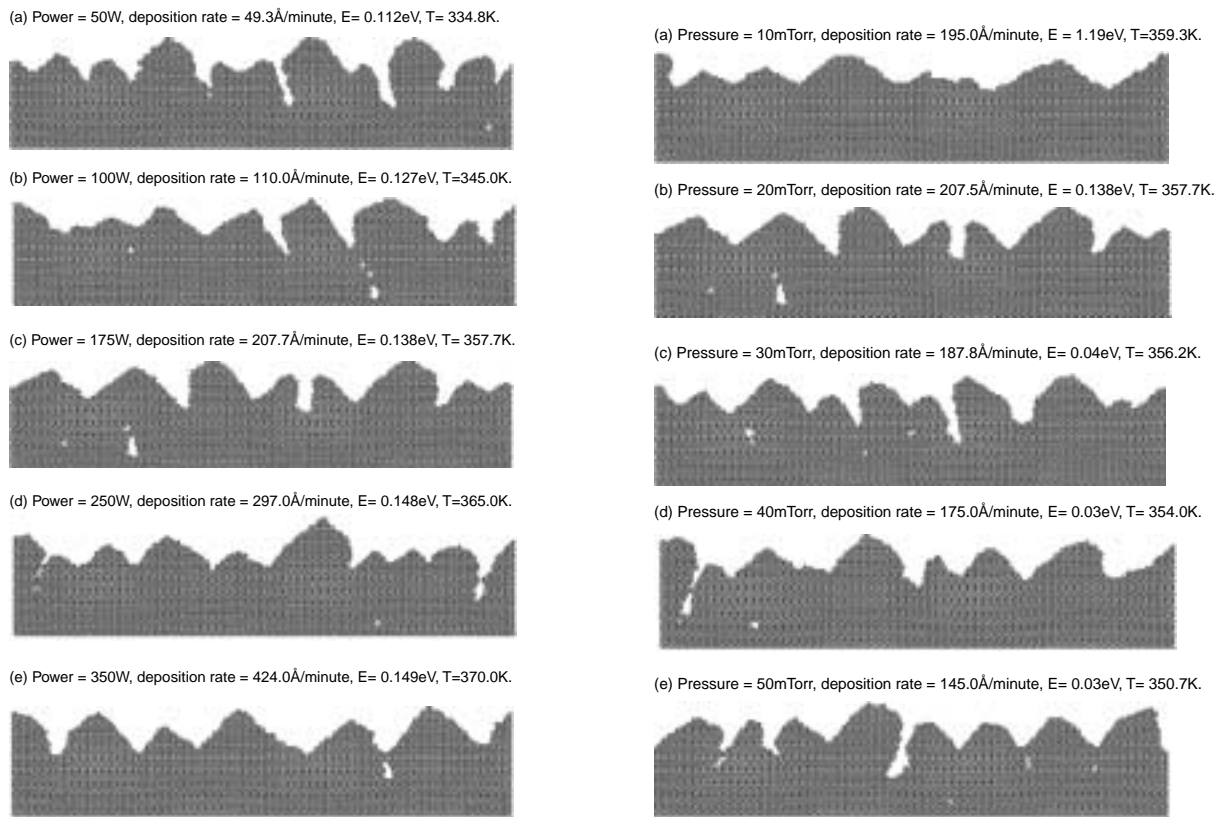


Figure 16. Comparison of HK-MC simulation and atomic force microscopy results for copper deposition showing (a) input power effect, and (b) pressure effect.

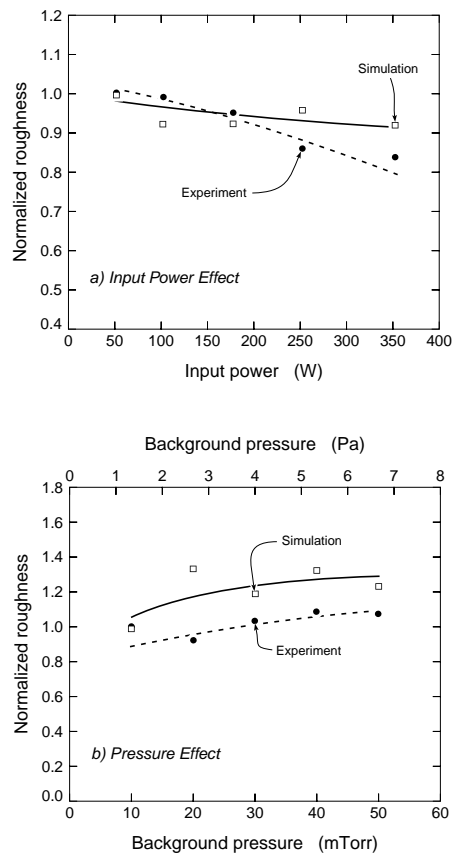


Figure 17. Comparison of measurement and simulation results for normalized film roughness showing (a) input power effect, and (b) pressure effect.

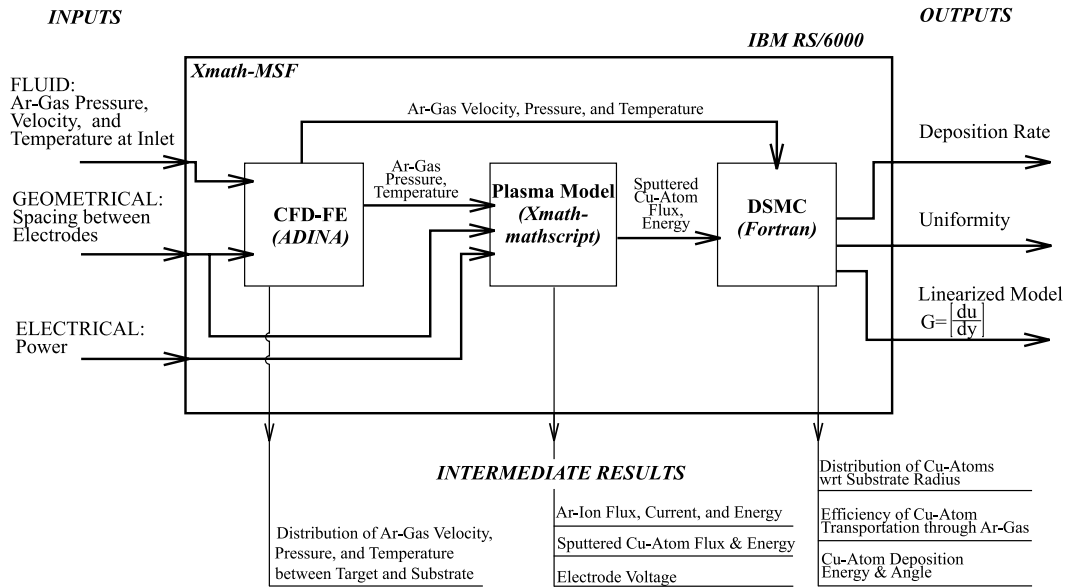


Figure 18. Virtual integrated prototyping (VIP) model for RF diode sputter deposition.

8. Integrated Flow/Plasma/Sputter/Transport Model

The individual models for gas flow, plasma discharge, copper sputtering, and DSMC-based copper atom transport were integrated to create a detailed Virtual Integrated Prototype (VIP) of the process depicted in Figure 18. The figure shows how the various individual models and their respective inputs and outputs are interrelated. Also shown in this figure are the overall inputs, overall outputs and useful intermediate results of the VIP. A simplified steady-state model was obtained by approximating the results of the fluid, plasma, sputter, and DSMC models with appropriate nonlinear curve-fits. This approximate model, coded in C, executes a simulation in about a second on a desktop computer, therefore facilitating quick exploration of the design space.

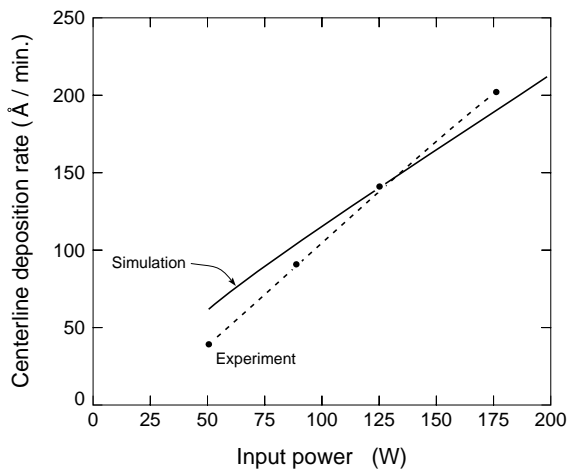


Figure 19. Comparison of experimental data and VIP model prediction of copper deposition rate as a function of input RF power.

The integrated model was validated against experimental data. Figure 19 shows that the approximate model yields results for the deposition rate as a function of power which are in good agreement with experiments.

Simulated sensitivity results from the integrated model are shown in Figure 20 in which the deposition rate is plotted as a function of the main input variables: power, gas pressure, gas temperature and electrode spacing. The results in Figure 20 show that increasing the input power can significantly increase the deposition rate. Sensitivity results for the effect of the input variables on the film thickness uniformity across the substrate are shown in Figure 21. The only variable that significantly affects uniformity is the electrode spacing with uniformity decreasing as spacing increases.

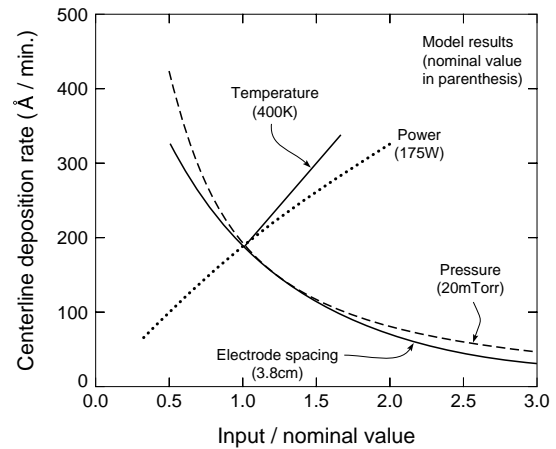


Figure 20. Sensitivity of the centerline deposition rate to variations in process parameters obtained from the integrated model simulations.

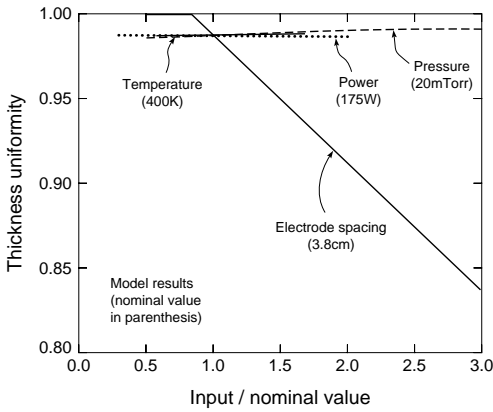


Figure 21. Sensitivity of thickness uniformity to variations in process parameters obtained from the integrated model simulations.

9. Set-Point Control Tolerances

One important application of the coarse grained, integrated input/output model, described in this section, is in the determination of allowable tolerances on the process input variables in order to meet a specified manufacturing tolerance on film thickness. For example, a critical layer in the GMR process is the copper thin-film whose thickness must be 15\AA with an average tolerance of $\pm 0.25\text{\AA}$. Since the nominal deposition rate for copper is $190\text{\AA}/\text{min}$, a 15\AA film takes 4.74 seconds to deposit. In order that the thickness tolerance specifications be met, the processing time window is 4.74 ± 0.08 seconds. Based on the steady-state sensitivities obtained from the plots shown in Figure 20, the tolerances shown in Table 2 (with respect to the nominal values shown) in each input variable will result in a 0.25\AA variation in film thickness in a nominal deposition time of 4.74 seconds.

The results of this sensitivity analysis reveal that very small changes in the input process parameters can cause the film thickness to exceed acceptable tolerance limits. Therefore, extremely tight control of inputs such as pressure and power is crucial to maintaining run-to-run repeatability. It is noted that in the above calculations only one variable was allowed to change at a time. In reality, the tolerance on each parameter would be smaller since all the process parameters would vary simultaneously from the nominal values.

Table 2. Range in each process parameter variation that is allowed for a maximum variation of $\pm 0.25\text{\AA}$ in the thickness of the 16\AA conduction (CuAgAu) layer in GMR multilayer wafers, assuming that the other parameters are kept constant at the nominal values.

	Tolerance (absolute)	Tolerance (%)
Power	$175 \pm 3.50\text{ W}$	2.0 %
Pressure	$20 \pm 0.28\text{ mTorr}$	1.4 %
Temperature	$400 \pm 6.2\text{ K}$	1.6 %
Electrode Spacing	$3.81 \pm 0.060\text{ cm}$	1.6 %

10. Within Wafer Uniformity

As discussed in Section 6, the deposition uniformity within the wafer is affected by changes in the electrode spacing, and to a lesser extent, by changes in the gas pressure. However, the 1D plasma model does not consider plasma non-uniformities, which reduce radial uniformity by increasing the radial temperature gradient and introducing a radial variation in the energetic ions reaching the target.

The gas is heated by the plasma, and this heat is transferred to the chamber walls, chuck, etc., by conduction, and ultimately transferred to the cooling water circulated through the pipes. The thermal power dissipated in the gas by the plasma is calculated as follows. The areas of the target and the substrate are 0.0324 m^2 and 0.0629 m^2 , respectively. The plasma model predicts ion current densities of $6.86\text{ A}/\text{m}^2$ and $0.77\text{ A}/\text{m}^2$ for the target and substrate, respectively. As a result, ion currents of magnitudes 0.222 A and $4.85 \times 10^{-2}\text{ A}$ flow to the target and substrate, respectively. The plasma model also predicts target and substrate sheath voltages of 672.0 V and 83.9 V , respectively. Hence, the power deposited to the target and substrate (the product of the current and the voltage) is 149.3 W and 4.1 W , respectively. Since the total power delivered to the plasma is 175 W , the power that heats up the gas must be the difference between this number and the total power deposited at the electrodes, *viz.*, 21.6 W .

To estimate the effect of radial non-uniformity in RF power on the gas temperatures, a simplified 2D axisymmetric dynamic model of the sputter chamber was developed. The model geometry and the grid are shown in Figure 22. The contact resistance between the chuck and the rest, and the tray and lower wall, are modeled using a gap of thickness 0.1 mm filled with argon. Similarly, the contact resistances between the target, dark shield, and the vertical wall is modeled as an argon gap of 0.1 mm . For boundary conditions, the bounding walls and the target, which are both water-cooled, are assigned 300 K . The upper (horizontal) part of the annular rest is also water-cooled and is assumed to be at 300 K . All the solids are made of stainless steel (thermal conductivity, $k = 60\text{ W}/\text{m}^2$), while argon's conductivity is $0.022\text{ W}/\text{m}^2$, close to that of air. The diameter of the cylindrical plasma is assumed to be identical to that of the target, *viz.*, $4''$, and the total thermal power input into the plasma is 20 W . The model was implemented in MATLAB™ [20]. Figure 23 shows the radial temperature profiles for three conditions: uniform plasma power, 5% non-uniformity and 10% non-uniformity (i.e., the power decrease linearly by 5% and 10% from the center to the edge of the plasma). The temperature difference from center to edge is about 1 K for uniform power, but increases to 3.5 K and 5 K as the non-uniformity in the thermalized RF power increases to 5% and 10%, respectively. Another important result was that the temperatures reached steady state in less than a second after the step increase in the

power from zero to 20 W. Consequently, the heat transfer process during deposition of even the thinnest layer (copper layer needing about 5 s) is effectively steady-state.

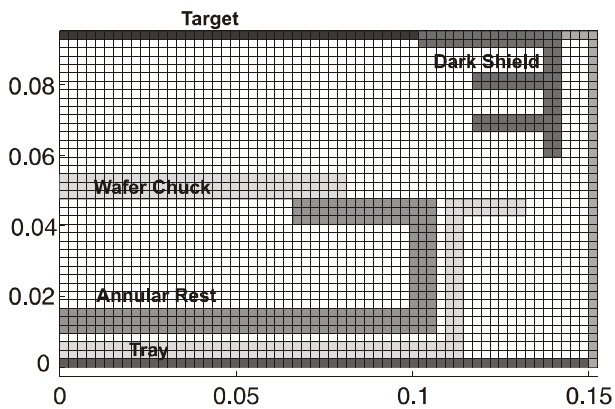


Figure 22. Grid used in the simplified 2D dynamic heat conduction model for sputter chamber.

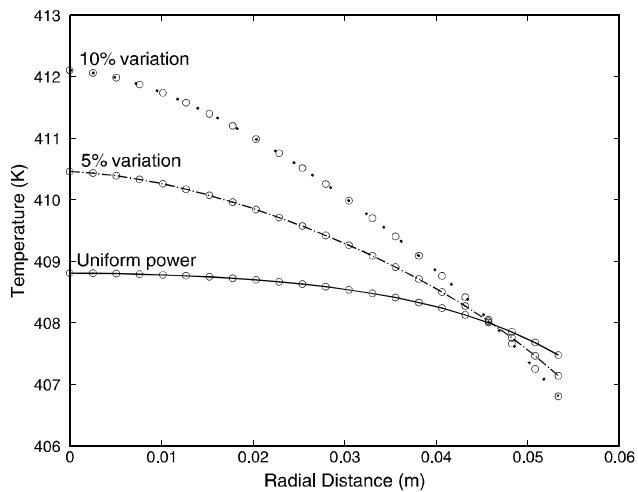


Figure 23. Radial temperature distribution within sputter chamber at a distance halfway between the anode and the cathode. The graphs to different radial non-uniformities in RF power delivered.

The calibration data for h_{sat} vs. thickness was used to compare model predictions with data. Effect of temperature variations is considered in an approximate manner by mapping the temperature variation to a deposition efficiency variation obtained from the sensitivity data in Section 9. Radial variation in the ion current to the target (and, hence, in sputtered atoms) caused by power non-uniformity are also considered. However, it is noted that we are essentially using sensitivities from the 1D plasma model for understanding approximate 2D behavior. A more accurate model of the non-uniformity would need a 2D plasma model and DSMC calculations with spatially varying temperature. However, the purpose of these calculations is to illustrate how substantial variations in h_{sat} may be caused by minor radial variations in plasma power.

Figure 24 shows the h_{sat} uniformity comparison with data for fourteen wafers (shown in gray). The measurements are made at five points along a diameter for each wafer, and the average h_{sat} for the fourteen wafers at each radial location is shown using a dark square. Non-uniform within the wafers is sufficiently high so that parts of the wafers have h_{sat} outside the tolerance band. The dark solid lines show the model prediction, with a radial plasma non-uniformity of 5%, at mean power settings of 172 W and 178 W. It is seen that a RF power input of 172 W, which causes a 5 K decrease in the average gas temperature from its nominal value of 400 K, would be sufficient to move most of the wafers out of the tolerance band. Figure 5 also shows the model predictions if plasma is considered to be uniform. These results emphasize the sensitivity of the wafer properties to small changes in the process parameters, and to radial non-uniformities in the plasma.

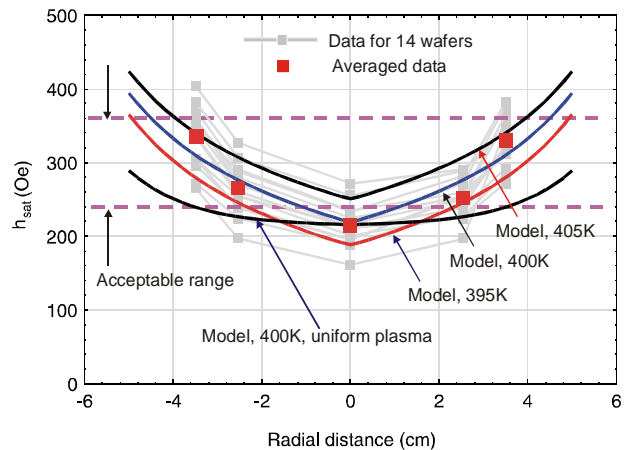


Figure 24. Effect of variation in gas temperature of 10 K on the saturation magnetic field 4'' GMR multilayer wafer. The same variation in h_{sat} would be caused by a 6 W variation in RF power. Data for fourteen wafers measured at five points along a diameter are also shown.

11. Improved Deposition Uniformity

Simulations using the integrated model indicated that the film thickness uniformity may be improved in two ways. As discussed in Section 6 (and shown in Figure 13), one way would be to reduce the electrode spacing. Experiments were conducted at NVE with the spacing being reduced to 1.3 in from the nominal setting of 1.5 in. The multilayer wafers were tested using NVE's standard thirteen-point pattern with sheet resistance, GMR, and h_{sat} being measured. Using the calibration data, the CuAgAu layer thickness was determined from the h_{sat} data using the average of the thirteen points. In Figure 25, the thickness along one diameter of the wafer was plotted (normalized against the center thickness), and compared with the integrated model predictions. The results showed that this closer spacing reduced the within-wafer standard deviation, σ , of h_{sat} by 45% while producing wafers with excellent GMR. NVE is studying incorporation of reduced electrode spacing into their process. The differences between the actual uniformity

and that predicted by the model are due to both model inaccuracies as well as measurement errors.

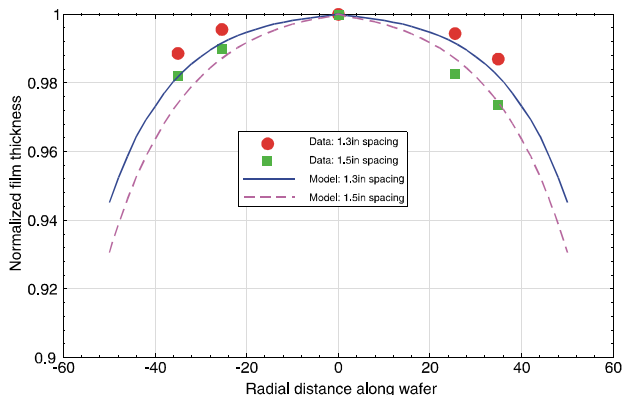


Figure 25. Experimental data on the effect of electrode spacing on deposition uniformity. Note that the y-axis range is 10%.

The second method to improve within-wafer thickness uniformity would be to shape target concave, since the reduced spacing at the edges would compensate for the flux of atoms escaping from the plasma boundary. The targets for the critical CuAgAu conducting layer for GMR multilayer wafers produced at NVE are made of copper and silver with gold tabs attached at several points on the target at various points using epoxy. A target was machined to a concave curvature of radius 0.7m with gold tabs installed on the surface in a pattern identical to the plane target. Figure 26 shows the film thickness uniformity, determined again from the h_{sat} vs. thickness calibration curve, and comparison with model predictions. Since the data is normalized against the center thickness, the data points at $x=0$ for all data sets coincide. It is seen that there is marked improvement in uniformity due to the use of concave targets. Extensive tests were subsequently performed at NVE to qualify the use of curved targets for regular production. Comparison of the curved target and standard target data showed that while there was little change in the GMR, both sheet resistance and h_{sat} uniformity decreased by 50% when the curved target was used. In addition, the multilayers grown with concave copper target were found to have superior temperature stability, probably caused by composition differences in the CuAgAu film. As a result of the successful

qualification runs, the curved target has been adopted for multilayer GMR wafer production at NVE.

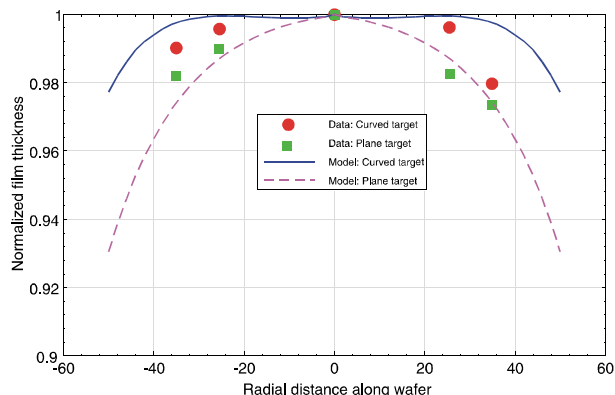


Figure 26. Experimental data on the effect on deposition uniformity of shaping of the target concave. Note that the y-axis range is 10%.

12. Conclusion

A reactor-scale model incorporating the principal physical processes involved in RF diode sputtering has been developed and then integrated into a detailed steady-state input-output model of the growth of copper films. The model links critical aspects of the process (plasma power and pressure), the geometry of the chamber, and the materials (working gas, target materials) to the surface morphology of thin metal films. Experiments revealed a strong dependence of the surface morphology upon power and pressure. The reactor scale model successfully predicted the functional form of these trends and therefore establishes a causal linkage between the method and conditions of processing and the morphology of the resulting thin film. The model has been coarse grained and used to investigate the sensitivity of the process outcome to the conditions of processing. Very small changes in process set point are found to significantly reduce control of film thickness. This observation is especially critical for efforts to grow GMR film where small variations in copper layer thickness lead to large variations in magnetoresistive properties. Finally, the use of a curved target, guided by simulations of the integrated model, led to substantial improvements in the within-wafer uniformity of sheet resistance and saturation field in qualification tests.

References

1. Levy, P.M., *Giant Magneto-Resistance in Magnetic Layers*, Solid-State Physics, Advances in Research and Application, Volume 47, Academic Press, San Diego, 1994.
2. Daughton, J. M. and Y.J.Chen, *GMR Materials for Low Field Applications*, IEEE Transactions on Magnetics, Vol. 29, No.6, November 1993.
3. Zou, W. *et al.* *Sputter Deposition of GMR Spin Valves*, MRS Symposium "Mechanisms, Models and Methods of Vapor Deposition", Edited by H.N.G. Wadley, G. Gilmer, W. Barker, MRS, 2000.
4. Schlichting, H., *Boundary-Layer Theory*, 7th ed. McGraw-Hill, New York, 1979.
5. Lieberman, M. A., and A. L. Lichtenberg, *Principles of Plasma Discharges and Materials Processing*, John Wiley and Sons, New York, 1994.
6. Integrated Systems, Inc., Matrix_x Product Family Users Manuals, Sunnyvale, California, 1996.
7. Urbassek, H. M., *Molecular-dynamics simulation of sputtering*, Nuclear Instruments and Methods in Physics Research B 122, pages 427-441, 1997.
8. Groves, J. F., *Directed Vapor Deposition*, Ph. D. Dissertation, University of Virginia, 1998.
9. Bird, G. A., *Molecular Gas Dynamics and the Direct Simulation of Gas Flows*, Clarendon Press, New York, 1994.
10. Somekh, R. E., *The thermalization of energetic atoms during the sputtering process*, J. Vac. Sci Technol. **A2**(3), p. 1285, 1984 .
11. Masoliver, J., Porrà, J. M., and Weiss, G. H., *Some two and three-dimensional persistent random walks*, Physica A, **193**, p. 469, 1993.
12. Massey, H. S. W., and Burhop, E. H. S., *Electronic and Ionic Impact Phenomena: Collisions of Electrons with Atoms*, Vol I, Clarendon Press, New York, 1969.
13. Robinson, R. S., *Energetic binary collisions in rare gas plasmas*, J. Vac. Sci. Technol., 16(2), p. 185, 1979.
14. Massey, H. S. W., *Electronic and Ionic Impact Phenomena: Slow Collisions of Heavy Particles*, Vol III. Clarendon Press, New York, 1971.
15. Zhou, X. W., *et al.*, J. Appl. Phys. 84, 2301 (1998).
16. Landau, L.D. and Lifshitz, E. M., *Mechanics*, 3rd edition, Pergamon Press, New York, 1976.
17. Yang, Y. G., Ph.D. Thesis, University of Virginia, May 2000.
18. Zhou, X. W., and H. N. G. Wadley, *Hyperthermal Vapor Deposition of Copper: Athermal and Biased Diffusion Effects*, Surf. Sc., **431**, pp. 42-57, 1999.
19. Zhou, X. W., and H. N. G. Wadley, *Hyperthermal Vapor Deposition of Copper: Reflection and Resputtering Effects*, Surf. Sc., **431**, pp. 58-73, 1999.
20. *MATLAB™*, The MathWorks, Inc., Natick, MA 01760.